Journal of Laser Applications

RESEARCH ARTICLE | NOVEMBER 10 2025

Application of multimodal process monitoring for enhanced quality control and defect detection in laser-based directed energy deposition

Cedric Hauschopp ; Simon Dicks ; Jan Bremer ; Daniel Wall; Gert Dehnen ; Nick Brierley ; Richard Kraft ; Thomas Schopphoven ; Wilhelm Meiners

J. Laser Appl. 37, 042035 (2025)
https://doi.org/10.2351/7.0001909

ALIA THE LASER INSTITUTE

Journal of Laser Applications ARTICLE pubs.aip.org/lia/jla

Application of multimodal process monitoring for enhanced quality control and defect detection in laser-based directed energy deposition

Cite as: J. Laser Appl. 37, 042035 (2025); doi: 10.2351/7.0001909
Submitted: 30 June 2025 · Accepted: 7 October 2025 ·
Published Online: 10 November 2025

Cedric Hauschopp,[1,a)] Simon Dicks,[1] Jan Bremer,[2] Daniel Wall,[3] Gert Dehnen,[3] Nick Brierley,[4] Richard Kraft,[1] Thomas Schopphoven,[1] and Wilhelm Meiners[1]

AFFILIATIONS

[1]Fraunhofer Institute for Laser Technology ILT, Steinbachstr. 15, Aachen 52074, Germany
[2]BCT Steuerungs- und DV-Systeme GmbH, Carlo-Schmid-Allee 3, Dortmund 44263, Germany
[3]Point 8 GmbH, Rheinlanddamm 201, Dortmund 44139, Germany
[4]Diondo GmbH, Ruhrallee 14, Hattingen 45525, Germany

[a)]**Author to whom correspondence should be addressed; electronic mail:** cedric.hauschopp@ilt.fraunhofer.de

ABSTRACT

Laser-based directed energy deposition (also known as laser material deposition, LMD) is an additive manufacturing (AM) process that uses laser radiation to create a melt pool on a component's surface while feeding filler material through a nozzle. LMD is established in various industrial applications for coatings, repairs, and AM. However, it involves numerous parameters, necessitating complex process management and expertise. Variable conditions, such as differing workpiece geometries, materials and varying powder quality, complicate the process, potentially leading to time-consuming and costly development efforts along with deviations in component quality. This work applies a multimodal process monitoring workflow to analyze and actively improve process behavior toward defect mitigation. Reference cubes built under nominal process parameters are compared to cubes deposited with varying laser power. During deposition, spatially synchronized data streams from a pyrometer, melt-pool camera, and optical coherence tomography are acquired. A laser scanner combined with post-build computed tomography provides 3D-defect masks that are co-registered with the process data. Extensive data analysis revealed a pronounced directional dependence. Based on these findings, additional test cubes are deposited using targeted, local parameter adjustments to mitigate the directional bias with an open-loop strategy.

Key words: LB-DED, LMD, process monitoring, data analysis, computed tomography

I. INTRODUCTION

Laser-based directed energy deposition for metals (DED-LB/M), also known as laser material deposition (LMD), is an additive manufacturing (AM) technique. The process involves generating a melt pool on a component's surface using laser radiation, while filler material is supplied through a nozzle. This method is well-established in industrial applications, particularly for coating, repair, and AM.[1–3] A schematic illustration of the process is shown in Fig. 1.

LMD is a complex process and necessitates expert knowledge due to variable boundary conditions and materials. This high complexity can lead to time- and cost-intensive parameter developments, as well as deviations in workpiece quality. To mitigate these issues, sensor-based process monitoring can contribute to ensuring process stability and identifying inconsistencies. Often used sensors include a pyrometer for measuring the melt pool temperature or a coaxial melt pool camera for recording the melt pool geometry and intensity.[2]

However, current methodologies primarily utilize individual sensors for process monitoring and control, which can—without complimenting measurements—result in misinterpretations and faulty controls.[2,4,5] These approaches attempt to keep a parameter

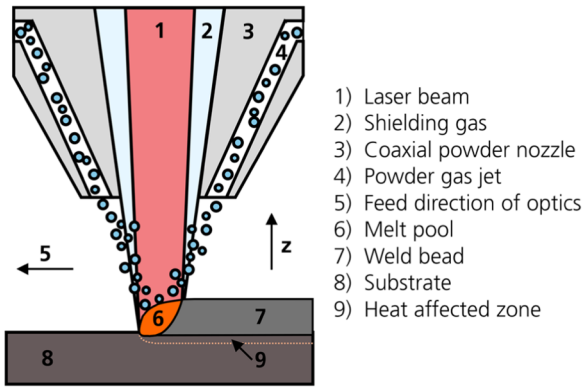

FIG. 1. Principle of LMD process.

constant, such as the melt pool temperature, without considering that data quality can be affected by geometric factors, incorrectly adjusted processes, or even worn-out nozzles. This leads to a low significance of the data, as its informative value is highly limited and its full potential is not exploited. Various approaches have already been considered for the control of the LB-DED process, in both closed-loop[6–8] and open-loop[6,9,10] control systems. The most commonly used parameter for controlling the process is the variation in laser power, as the laser power is easy to modify and usually responds with low latency.

First approaches for spatially resolved process monitoring exist,[11,12] where sensor data are synchronized with a tool center point. Further, CT analyses have been used to correlate data from sensors with the formation of defects.[12–14] However, it has not yet been demonstrated that a combination of complimenting spatially resolved data streams and subsequent CT analyses can actively prevent defects in open-loop control. Therefore, the approach presented in this work employs a multivariate process monitoring system, previously presented in a prior study,[15] which serves as the basis for an open-loop strategy. The system synchronizes multiple, spatially resolved data streams and offers a process chain for an accurate location-based superposition of sensor data and CT-based defect masks.

The monitoring system is used to systematically reveal process anomalies through comprehensive data analysis. Process data are recorded during the deposition of various cubes. Once an understanding of the data has been gained, systematic parameter changes are made to map the influence between parameter changes and the formation of defects in the data. In a final study, an attempt is made to vary the parameters locally in order to control the formation of defects at specific layers.

II. EXPERIMENTAL PROCEDURE

A. DED-LB/M manufacturing of coupons

For the validation of the multimodal process monitoring, coupons with a size of $20 \times 20 \times 10\ \text{mm}^3$ are deposited. All experiments are carried out on a KUKA 6-axis robot of the type KR90 R3100 HA with a KRC4 controller and a Precitec YC52 optical system. As a beam source, a Laserline LDF 5000–30 diode laser with a wavelength of $\lambda = 940–1060$ nm and a top-hat intensity distribution at a laser beam diameter of $d_L = 1.6$ mm are employed. A coaxial powder nozzle of type HighNo 4.0 by HD Sonderoptiken GmbH with a nominal standoff distance of 9 mm is utilized for the powder supply. The setup is shown in Fig. 2.

The powder material used in this study is AP&C Nickel718, which is similar to Inconel®718 (IN718). The chemical composition of the powder is summarized in Table I. As substrate material, AISI 304/EN 1.4301 is used.

The parameters were predetermined on individual tracks and intentionally not optimized for volume build-up to increase the potential for inducing defects. An overview of the parameters employed can be found in Table II.

For the experimental study, five reference cubes are initially built (Series A). In the next test series (Series B), the laser power is then reduced and increased by 200 W, respectively, to examine the influence of the laser power on process data and defect formation. Based on the results of Series B, the laser power is then changed depending on the layer to influence the defect formation locally (Series C). The magnitude of the laser power variations is based on knowledge gained from Series B. Between every test series of the study, the alignment of the nozzle is recalibrated against the laser focal point. For this recalibration, screws on a nozzle adjustment unit are aligned, which moves the nozzle in the XY plane. This was necessary due to ongoing laboratory work between the test series. The sample labels are listed in Table III.

The build-up strategy for the cuboids involves contouring followed by a bidirectional hatching. The distance between the contour movement and the tracks corresponds to the hatch distance y_D listed in Table II. For hatching, fly-ins/outs with a length of 20 mm are employed. After each layer, the build-up is rotated by 90°. The path planning is done using the BCT OPENARMS software. The build-up strategy is illustrated in Fig. 3.

B. Data acquisition

A laser line scanner, which is mounted laterally to the optics, is used to capture the substrate geometry prior to welding and to obtain the actual cube geometry after deposition. To capture the process signature, the optical system is equipped with contactless sensors coaxial to the beam path. A list of all used sensors is provided in Table IV.

The size and intensity of the melt pool is determined using a CMOS camera. The camera captures monochrome 8-bit images at a frame rate of 60 FPS and a resolution of 1602×1202 pixels. A region of interest measuring 500×500 pixels is defined to capture the melt pool, mainly to eliminate unwanted nozzle reflections from the image.

To measure the temperature in the area of the melt pool, a quotient pyrometer with a wavelength of $\lambda = 1650–2100$ nm is employed. The spot size is set to $d_P = 3$ mm to achieve robust and less saturated measurements. To compensate for the loss of power, remelting tests on Inconel® 718 are conducted, and the emissivity ratio is determined to be $\varepsilon_V = 1.012$.

To measure the height of the deposits, an OCT sensor with a wavelength of $\lambda = 1550$ nm and a measurement spot diameter of

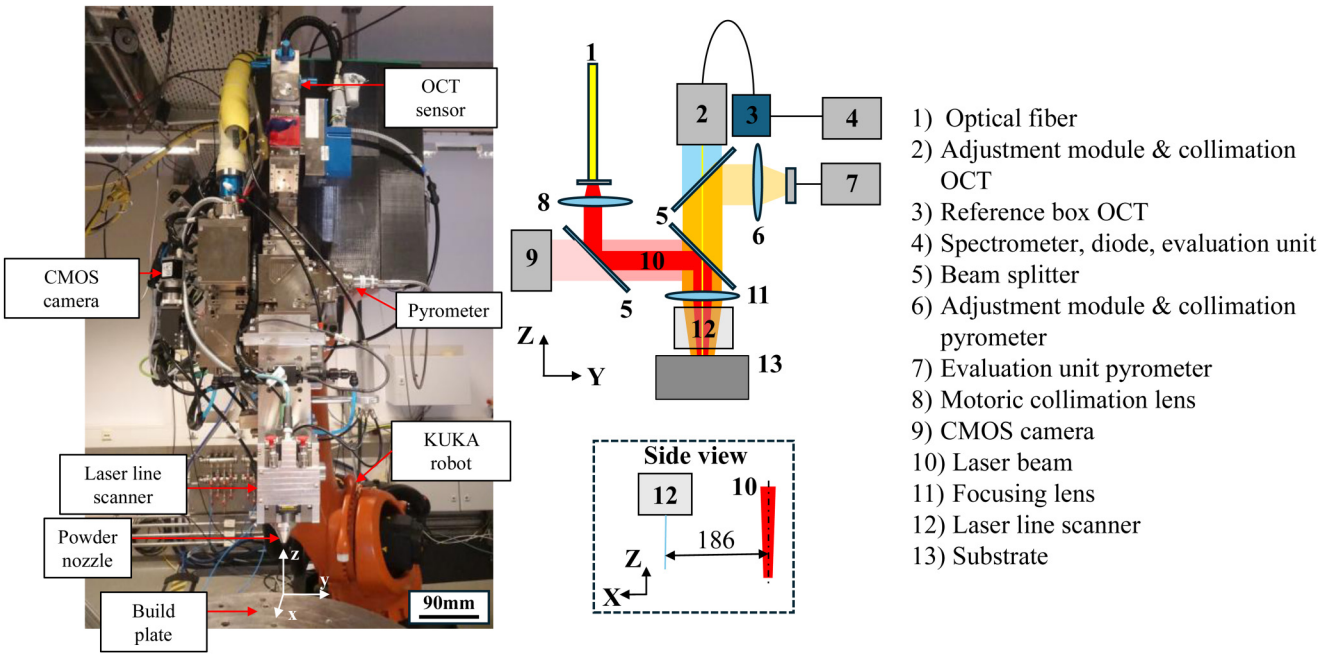

FIG. 2. Setup for welding of test coupons. Robot with optical system and implemented sensor technology [based on Hauschopp *et al.*, Werkstattstechnik Online **115**, 352–360 (2025). Copyright 2025 Author(s), licensed under a Creative Commons Attribution (CC BY) license].

$d_O = 50\,\mu$m is applied. The alignment of the measurement spot to the laser beam is achieved by traversing solid circular tracks followed by a displacement of the spot until no periodic influences are observable in the deflection of the measured value. A median filter is applied to the captured point cloud. The resulting measurement value reflects an absolute distance. An increasing height of the deposition and, therefore, a smaller standoff between nozzle and component corresponds to a lower distance signal. Measurements outside the measuring range are evaluated as 0 mm standoff.

Measuring data are captured using a National Instruments cDAQ 9185 data acquisition module and synchronized with the robot's position data from a KUKA Fast Send Driver module at a measurement frequency of 1 kHz.

For the computed tomography scans, a Diondo d2 microfocus CT system with a tube voltage of 240 kV and an area detector with a resolution of 3000 × 3000 pixels are utilized.

C. Data analytics

With the existing setup, data can be recorded with spatial resolution. In order to analyze only the data points where the laser is turned on, the trigger signal of the laser is recorded and used as a filter.

While the measured values from the OCT sensor and the pyrometer are not processed any further, the images from the CMOS camera are analyzed using the *Sum intensity* value according to Eq. (1),

$$\text{Sum intensity} = \frac{\sum_{i=1}^{N} I_i}{I_{\max}}. \tag{1}$$

The intensity values I of each pixel are normalized with respect to the maximum possible intensity I_{max}.

All data interfaces are linked to the OPENARMS software from BCT GmbH. The wide range of interfaces enables all steps relating to the whole data acquisition process chain, path planning, as well as the geometry scans to be spatially synchronized and correlated

TABLE I. Composition of AP&C Nickel 718 in nominal wt. %.

Ni	Cr	Mo	Fe	Nb + Ta	Co	Al	Ti
Bal.	19	3	18	5.1	0.95	0.5	1

TABLE II. Reference parameters for IN718 coupons.

Laser power P_L (W)	960
Process feed rate v_f (mm/min)	2000
Powder mass flow $\dot{m}_P$ (kg/h)	0.6
Hatch distance y_D (mm)	0.8
Layer offset Δz (mm)	0.78
Shielding gas flow Qs (l/min)	10
Carrier gas flow Qc (l/min)	3.5

TABLE III. Samples of experimental study including the pattern for laser power for experiments with layer-based laser regulation.

Sample no.	Laser power: Difference to $P_{L,\ Ref}$ (W)	Laser power: Pattern for X [W] Layer 1;2;3;4 (periodic)
Series A		
Ref1–Ref5	0	—
Series B		
Ref6, Ref7	0	—
$P_{L,\ Ref} - 200\_1$; $P_{L,\ Ref} - 200\_2$	−200	—
$P_{L,\ Ref} + 200\_1$; $P_{L,\ Ref} + 200\_2$	+200	—
Series C		
Ref8	0	—
PL, Ref-200_3	−200	—
P-200 + VAR1	−200 + X	100; 80; 0; 0
P-200 + VAR2	−200 + X	150;100; 0; 0

TABLE IV. Applied sensors with specifications and associated measurands.

Sensor	Specification	Measurand
CMOS Camera (Basler acA1600–60g m)	Frame rate: 60 fps Picture resolution: 1602 × 1202 px	Melt pool size and -intensity
Quotient Pyrometer (Mergenthaler LASCON LPC04)	Temperature range: 250–3000 °C Accuracy: <1500 °C: 0.5% ± 2 K Frequency: 10 kHz Wavelength: 1.65–2.1 μm (2-color)	Melt pool temperature
Low-coherence interferometer (Precitec IDM1550 SD-OCT)	Wavelength: 1550 nm Sensor resolution: 10 μm Frequency: 70 kHz	Deposition height
Laser line scanner (μ-epsilon 2950-BL)	Measuring range: 50 mm Sensor resolution: 4 μm ± 0.008% (in z)	Substrate and workpiece geometry

with CT data. For this reason, the geometry scans, which are carried out after the deposition of the coupons, are overlaid with the generated CT defect masks. The masks are transferred to the coordinate system of the scans—and, therefore, to the process data—and aligned via the least square algorithm. The alignment can be adjusted for specific applications and is carried out at selected reference points, which in this case are set on the cube surface. This ensures a good fit in the evaluation area and prevents invalid results. A rigid body transformation is calculated for a minimum distance to the geometry scan. Using this algorithm, an average alignment residuum of <100 μm was achieved in a previous study,[15] exemplified using Fig. 4.

III. RESULTS AND DISCUSSION

A. Reference cubes

The deposited coupons are shown in Fig. 5. The cubes are built up with uniform quality. Although the cubes show good geometric accuracy, a slight rounding at the upper edges is noticeable, which results from a combination of surface tension and insufficient contouring material. A height measurement of the cubes results in an average height of 11.02 ± 0.10 mm. This corresponds to a deviation of 0.1 mm from the target height of 10.92 mm.

The acquired process data for the reference cubes are shown in Fig. 6. To avoid outliers, the median value across the layers of the cube is shown in each plot.

The OCT signal shows an almost constant standoff between nozzle and substrate with a slight downward trend across the layers of the cubes, with maximum deviations <0.25 mm per cube. This suggests that the layer increment is selected appropriately, while the OCT value corresponds to the order of magnitude of a height deviation of 0.1 mm. As is known from the literature, a slightly smaller standoff between powder nozzle and workpiece leads to a self-regulating process.[16] Since the cubes are built slightly too high, the standoff remains stable. For sample Ref1 in particular, it can be

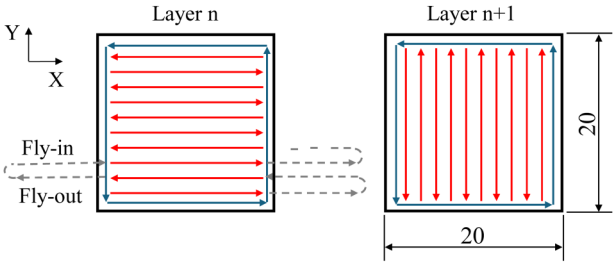

FIG. 3. Build-up strategy for coupons.

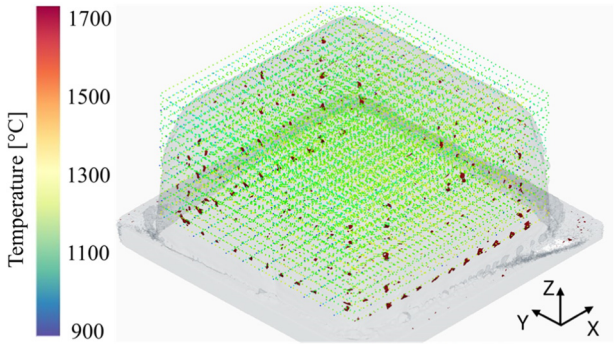

FIG. 4. Exemplary overlay of process and CT data by using a geometry scan and BCT OPENARMS software [based on Hauschopp *et al.*, Werkstattstechnik Online **115**, 352–360 (2025). Copyright 2025 Author(s), licensed under a Creative Commons Attribution (CC BY) license].

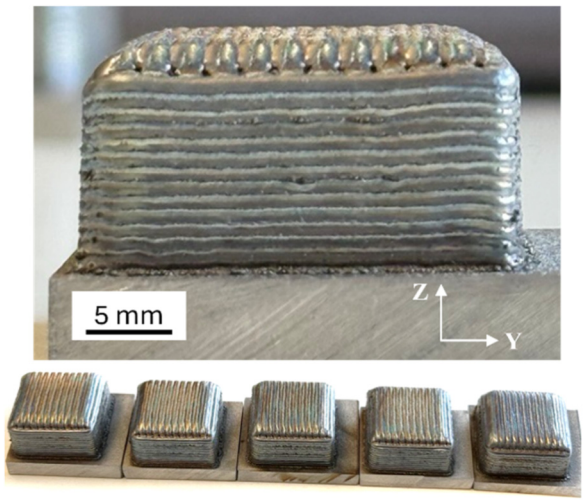

FIG. 5. Coupons deposited with reference parameters.

seen that the median value changes marginally after each layer. This can be explained by the change in welding direction between the X and Y axes.

In Fig. 7, the spatially resolved OCT data of sample Ref1 are shown. The data show lower distance values for the edge areas, which increase over the height of the cube. As can be seen on the top surface, the center area shows a smaller standoff distance, which gradually decreases to the outside areas. The data, therefore, represent the actual shape of the cubes, where the geometry flattens out at the edges.

In a direct comparison of the cubes, similar median temperatures are measured in the pyrometer signal. However, there is a clear periodicity that is measured in all cubes and does not appear in the OCT measured value. It is noticeable that the extrema are measured with a periodicity of 4. This is consistent with the direction-dependence of the layers, which is repeated every four layers due to the 90° rotation. Possible causes could be an incorrect alignment of the pyrometer to the laser beam, a direction-dependent powder supply, or an axis-dependent movement of the robot. It is also noticeable that the tendency of the median temperature decreases with increasing component height. This is contrary to the expected continuous heating of the cube due to reduced thermal conduction with increasing height. One reason could be the rounding of the edges, which leads to the pyrometer's measuring spot measuring further outside the cube with increasing build height.[15] Although the welding results indicate a stable process, there are fluctuations in the median temperature between the cubes of up to 60 °C.

By adding the images from the CMOS camera to the analysis, the periodicity can be confirmed. The analysis of the sum intensity shows a similar pattern to the pyrometer measurement, which means that the pyrometer adjustment can be ruled out as the main cause for the direction dependency. A periodicity can also be determined every four layers, whereby the extrema occur approximately

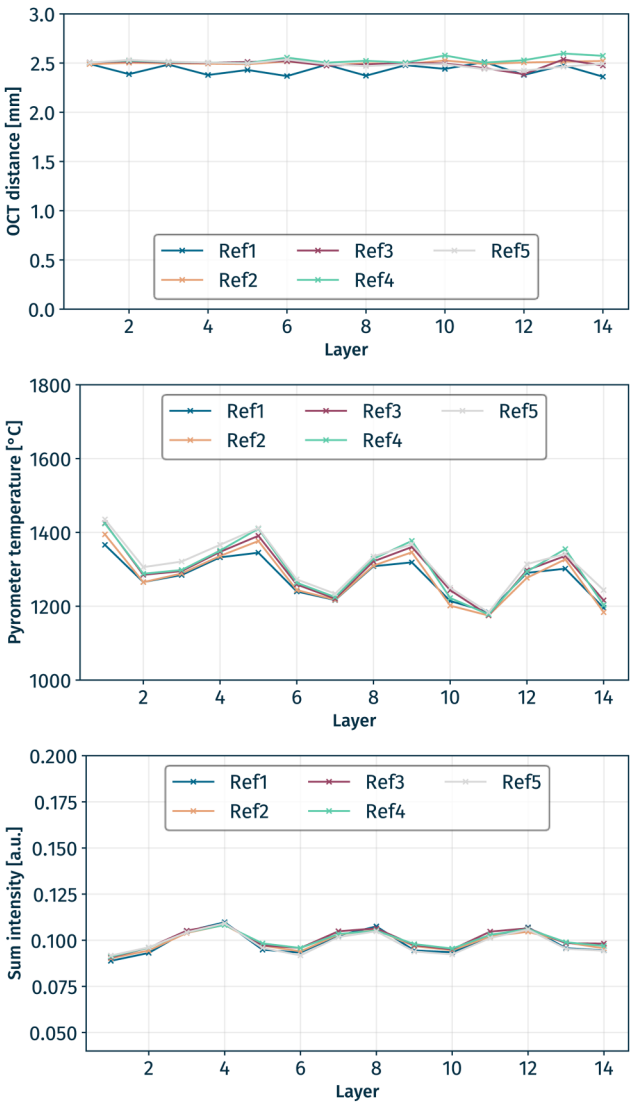

FIG. 6. Measured layer-based median values of reference coupons Ref1–Ref5 (Figure: Point 8).

one layer earlier compared to the pyrometer signal. Further, there is an increasing trend in the melt pool intensity, which is more consistent with the heating of the cubes described above, since a hotter melt pool usually corresponds to a higher intensity or a larger melt pool surface. Over a sample of five cubes, the deviations between the cubes are significantly smaller than the amplitude of the periodicity. This shows a high reproducibility of the process, but a strongly periodic behavior of the process stability, which is not visible in the welded samples.

In addition to the cubes, circular paths are welded in order to investigate the direction dependency in detail and to exploit the potential of spatially resolved process monitoring. For statistically

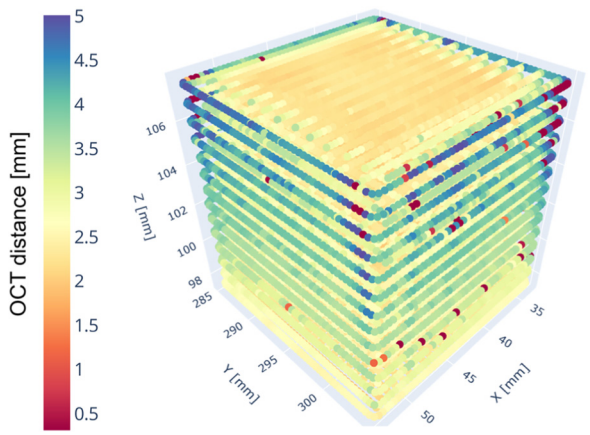

FIG. 7. Spatially resolved OCT data of sample Ref1.

usable data, circular paths with 10 adjacent tracks are welded for 3 layers. The measurement data of the pyrometer and the sum intensity of the CMOS images depending on the circular orientation are shown in Fig. 8. Both measurements clearly show that direction dependency is already present from the first track in the first layer. This means that the direction dependency is not influenced by previously welded tracks or layers. Further, it can be seen that the direction dependency between the two sensors is shifted in the orientation and a clearer decrease in amplitude can be observed in the pyrometer signal.

B. Variation of laser power

In order to significantly influence the process stability, cubes with a laser power of $P_L = P_{L,\ Ref} + 200$ W and $P_{L,\ Ref} - 200$ W are built. To obtain a direct reference, two new reference cubes are welded during the same test period.

An evaluation of the build height resulted in an average height of 10.8 mm for the $P_{L,\ Ref} + 200$ W cubes and 10.6 mm for the cubes with $P_{L,\ Ref} - 200$ W. It is noticeable that Ref7, with a height of 10.5 mm, is significantly lower than expected, while Ref6 has a height of 10.9 mm, which is significantly closer to the reference height. Visually, there are no significant differences between the reference and the power-modified cubes, but there is a slight porosity on the upper side of the low-power cubes. The evaluation of the sensor signals from the OCT sensor, the pyrometer, and the sum intensity of the CMOS images is shown in Fig. 9.

The distance value of the OCT signal shows a steady upward trend across all samples, with a maximum distance increase of approximately 0.4 mm for sample Ref6. While no clear correlation between laser power and distance value can be seen, a different trend compared to Series A is observable. This can be explained by a slightly different calibration of the nozzle or nozzle wear between test series. Sample Ref7 can be considered an outlier. The lower distance value results from many measurements outside the OCT range.

The pyrometer signal shows a clear correlation between the measured temperature and the set laser power. The periodicity of

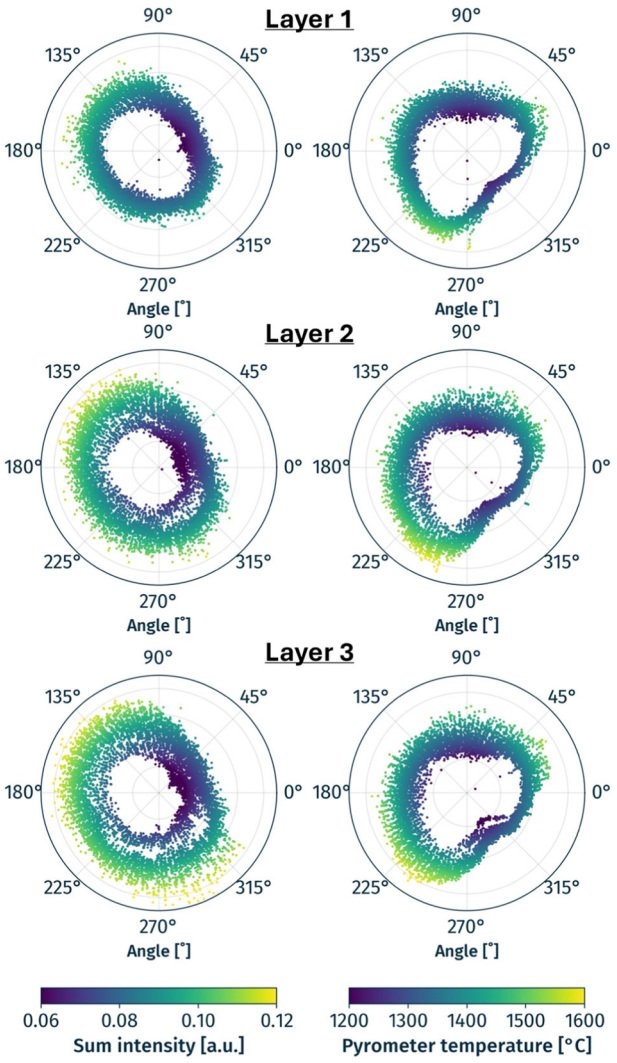

FIG. 8. Measurements of pyrometer temperature and CMOS image intensity dependent on circular orientation (Figure: Point 8).

the test series is consistent with the reference cubes Ref1–Ref5 and is, therefore, not significantly influenced by the laser power or the alignment of the nozzle. While the graphs for the power-modified cubes are evident, the reference cubes show an unclear pattern. This is first due to the outlier in sample Ref7, but also to the previously mentioned fluctuations in the median temperature, which were already observed in the reference cubes.

The correlation becomes more apparent in the sum intensity value of the CMOS images, whereby a higher laser power is associated with a higher intensity value. While the temperature of Ref7 decreased significantly during the build-up, the intensity is only slightly decreased compared to Ref6. By averaging the intensity values, it can be roughly estimated that a laser power of $P_L = 200$ W corresponds approximately to an intensity delta of 0.02–0.03 a.u.

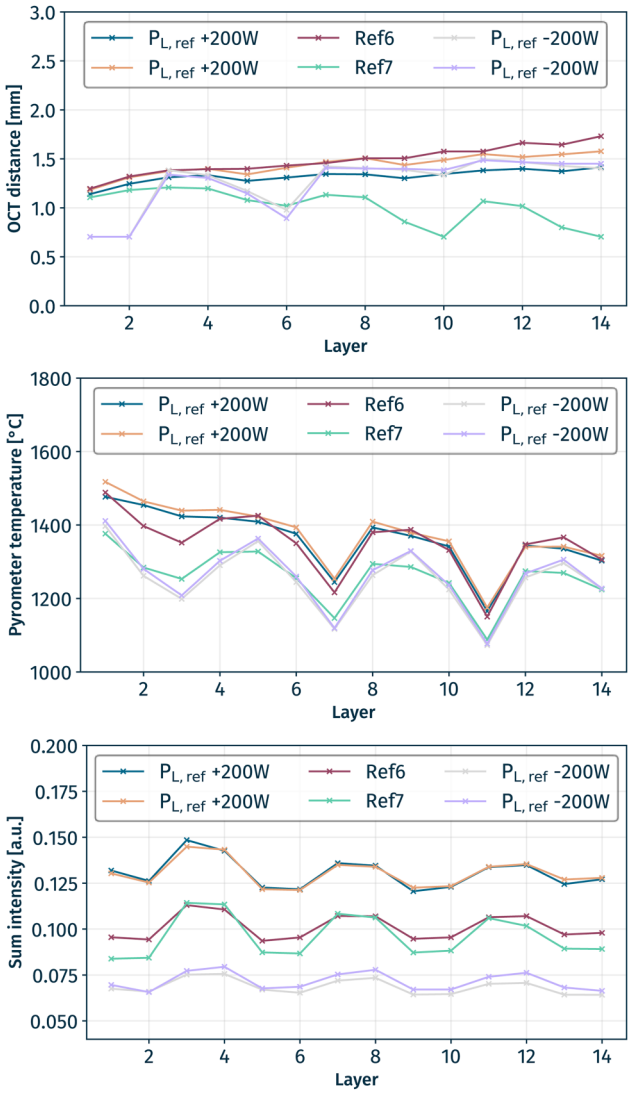

FIG. 9. Process data for cubes deposited with laser power variations (Figure: Point 8).

Based on the knowledge gained, cubes are welded a third time, and the laser power is adjusted layer by layer. The laser power steps of the analyzed samples are shown in Table III, whereby the pattern is repeated every four layers, starting at $P_L = P_{L,\,Ref} - 200$ W. Since the amplitude of the periodicity in the CMOS images approaches 0.01 a.u., laser power values around 100 W are estimated for the sample P-200 + VAR1 to compensate for the periodicity. To enhance the effect of the compensation, a slightly higher power compensation between 100 and 150 W is applied in the P-200 + VAR2 sample.

The sample Ref8 has a height of 10.9 mm and P-200 has 10.8 mm, while P-200 + VAR1 and P-200 + VAR2 have a height of 10.9 and 10.8 mm, respectively. The measured values of the OCT distance value, the pyrometer temperature, and the sum intensity of the CMOS images are shown in Fig. 10.

Starting with the OCT signal, constant results similar to reference samples Ref1–Ref5 are observed. Sample Ref8 is noticeable, with a consistently lower, but even OCT distance value, which cannot be explained without further investigation.

The pyrometer signal shows a downward trend in temperature for all samples, with an overall temperature drop of approximately 70 °C. In the reference sample, it can be seen that periodicity is detected again, although the amplitude is slightly lower than in the previously built reference samples.

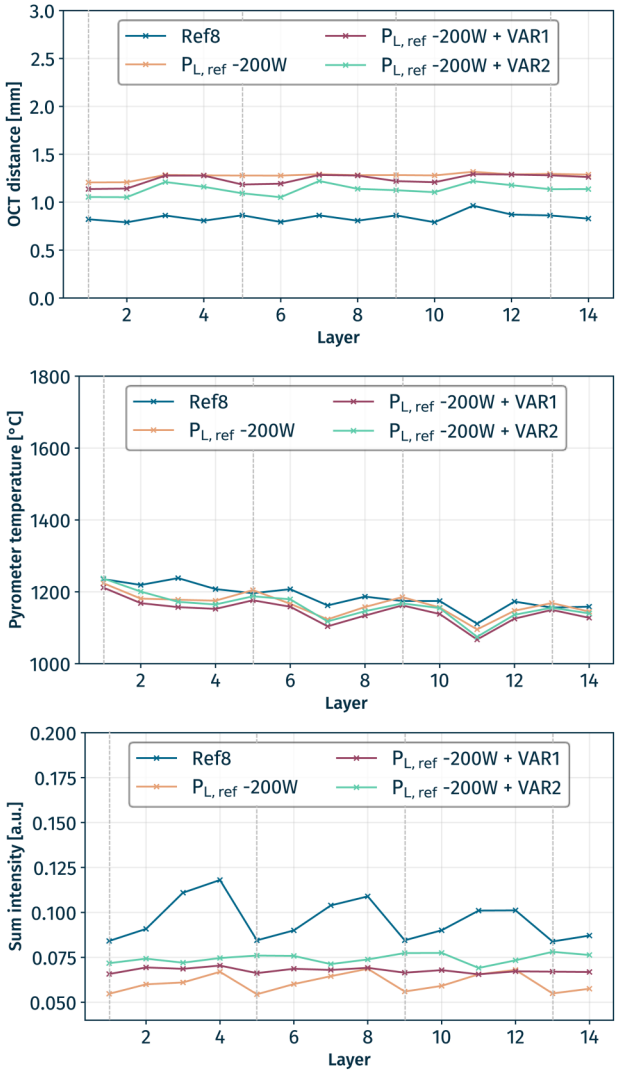

FIG. 10. Process data for cubes deposited with layer-based laser power variations. Onset of each period indicated by vertical gray lines (Figure: Point 8).

Likewise, no improvement in periodic process stability can be seen due to the layer-based laser power variation. The amplitude has decreased, but this can be put into relativity by the reference sample.

The sum intensity value of the CMOS images shows opposite results. While the values of the reference sample show similar peaks to those in the last test series, the layer-based power variation results in a significant reduction of the peaks. The effect is slightly

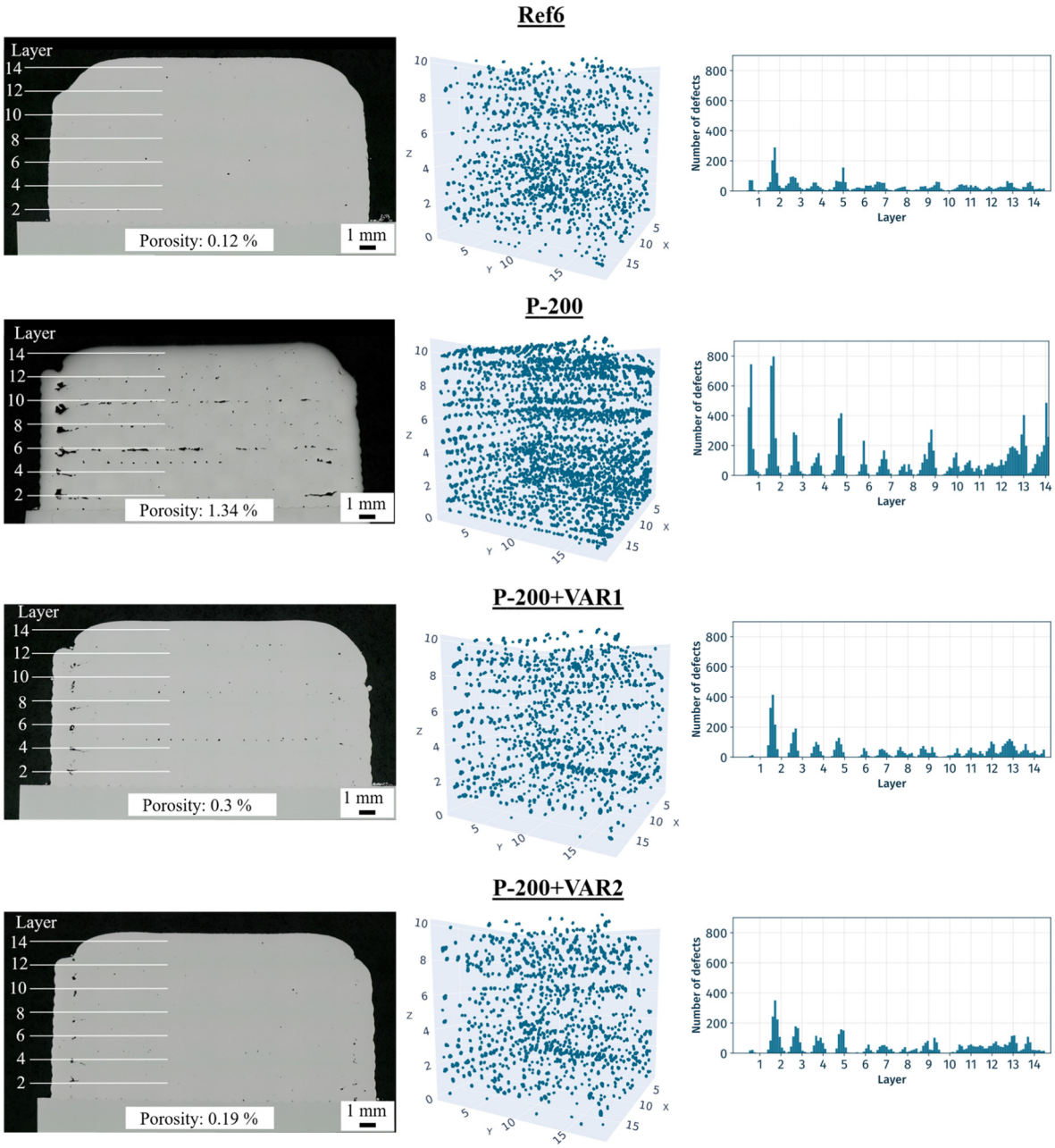

FIG. 11. Metallographic cross sections (left), spatial CT data (center), and histograms of CT defect distribution (right) of samples with layer-based laser power variation. (Cross sections: Fraunhofer ILT, Figures: Point 8).

stronger in the $P_{L,\ Ref}$ −200 W + VAR2 sample, as the intensity is even overcompensated.

C. Spatially resolved defect correlation

In the experiments of layer-based laser power variations, an open-loop control approach is used to find a defect-based correlation with the process data. Figure 11 shows defect masks based on the CT analyses of the test series. In addition, histograms are shown that represent the number of defects across the layer ranges.

The reference sample shows an even distribution of defects with an average number of 200 defects across the layers. It can be seen that the number of defects is higher up to layer 5. This is to be expected, as the cube heats up with increasing height and any porosity, therefore, has more time to degas in the higher layers. The metallographic cross section confirms a low porosity of 0.12%.

Sample P-200 shows a significantly higher defect density in comparison, measuring a porosity of 1.34%. The reduced applied laser power leads to the formation of pores and bonding defects between the tracks or layers. It is also noticeable that large defects occur in the left area of the metallographic cross section. This can be explained by the distance between contouring and hatching. As can be seen in the CT histogram, an increased number of defects is evident in the first layers. Further, an increased occurrence of defects in the top layer could be caused by a lack of remelting by the layers above. A clear periodicity is evident in layers 1, 5, 9, and 13. This corresponds to the periodicity of the intensity from the CMOS images, where local minima were measured.

In the samples with layer-based power adjustment, P-200 + VAR1 and P-200 + VAR2, this porosity is significantly reduced, although the laser power adaption toward the reference power is only performed in parts of the samples. An increased number of defects is also evident in the first layers, while very few defects are present in the top layer. This is likely due to the increased power in the last two layers, which results from the laser power pattern every four layers.

IV. CONCLUSION

In the presented work, a multimodal process monitoring system was applied for the manufacturing of coupons in an LB-DED process. In an open-loop approach, process data were used to actively prevent the formation of defects. Spatially resolved data from an OCT sensor, a pyrometer, and a coaxial CMOS camera were evaluated and correlated to post-build CT defect masks.

Overall, the following findings were collected:

- While a coaxial OCT sensor can be used to map the geometry of welded workpieces with high accuracy, it is less suitable for measuring direction-dependent effects. It gives an accurate view over the workpiece standoff and helps to classify other sensor signals that have geometry-related measured values.
- The pyrometer and the intensity of the pixel values from CMOS melt pool images enable weld direction-dependent periodicities to be detected in the process, which—under stable process conditions—cannot be determined from the welded samples or metallographic evaluations.
- The influence of laser power can be detected by both CMOS intensity and the pyrometer temperature. The pyrometer temperature shows greater fluctuations than the intensity of the CMOS images.
- Measured periodicities can be significantly compensated by adjusting laser power locally in individual layers. The level of compensation can be estimated using intensities from CMOS images.
- Slight data inconsistencies remain and require further investigation.

The measured process data were automatically superimposed with CT-based defect masks to establish a correlation with local defect formation. The following findings were gathered:

- Measured periodicities are directly reflected in the component quality when leaving stable process conditions. This can be confirmed by both metallographic images and CT scans.
- If periodicities in process data are compensated by local power adjustments, local defect formation can be prevented, which has been shown to decrease the porosity by more than 1%.

Building upon these findings, the applicability of the open-loop control system presented in this work may be extended to more complex geometries and relevant industrial use cases. With the systematic generation of adequate training datasets and the development of advanced AI models, it appears feasible to evolve this strategy into a closed-loop control framework capable of preventing defect formation *in situ*. Moreover, the presented approach can already be employed to design calibration procedures (as shown for circular tracks) that enable a rapid assessment of potential directional dependencies or deviations in nozzle standoff.

ACKNOWLEDGMENTS

This research and development project is funded by the German Federal Ministry of Education and Research (BMBF) as part of the program "Zukunft der Wertschöpfung—Forschung zu Produktion, Dienstleistung und Arbeit" (funding code 02P20A082) and supervised by the Project Executing Organization Karlsruhe (PTKA). The authors are responsible for the content of this publication. The authors would like to thank all project partners of the ProSLAM project for their outstanding cooperation and excellent results: BCT Steuerungs- und DV-Systeme GmbH, Point 8 GmbH, Diondo GmbH, Resolto GmbH, Precitec GmbH & Co. KG., and Fraunhofer ILT.

AUTHOR DECLARATIONS

Conflict of Interest

The authors have no conflicts to disclose.

Author Contributions

Cedric Hauschopp: Conceptualization (lead); Methodology (lead); Writing – original draft (lead). **Simon Dicks:** Conceptualization (supporting); Writing – original draft (supporting). **Jan Bremer:** Visualization (supporting); Writing – review & editing (equal). **Daniel Wall:** Visualization (lead). **Gert Dehnen:** Visualization (lead). **Nick Brierley:** Investigation (equal). **Richard Kraft:**

Visualization (supporting). **Thomas Schopphoven:** Supervision (lead). **Wilhelm Meiners:** Writing – review & editing (equal).

REFERENCES

[1]R. Poprawe, C. Häfner, and R. Wester, *Tailored Light 2* (Springer International Publishing, Cham, 2024).

[2]D.-G. Ahn, "Directed Energy Deposition (DED) process: State of the art," Int. J. Precis. Eng. Manuf.-Green Technol. **8**, 703–742 (2021).

[3]T. Schopphoven, "Experimentelle und modelltheoretische Untersuchungen zum Extremen Hochgeschwindigkeits-Laserauftragschweißen," Dr.-Ing. dissertation, Fraunhofer-Institut für Lasertechnik ILT; Fraunhofer IRB-Verlag, Aachen, 2019.

[4]L. Song, V. Bagavath-Singh, B. Dutta, and J. Mazumder, "Control of melt pool temperature and deposition height during direct metal deposition process," Int. J. Adv. Manuf. Technol. **58**, 247–256 (2012).

[5]R. Bernhard, P. Neef, H. Wiche, V. Wesling, C. Hoff, J. Hermsdorf, and S. Kaierle, *Entwicklung Einer Intelligenten Prozessüberwachung und Regelung zum Laserauftragschweißen von Multimaterial-Verbindungen* (Shaker Verlag, Düren, 2021).

[6]M. Mazzarisi, A. Angelastro, S. L. Campanelli, V. Errico, P. Posa, A. Fusco, T. Colucci, A. J. Edwards, and S. Corigliano, "Monitoring of directed energy deposition laser beam of nickel-based superalloy via high-speed mid-wave infrared coaxial camera," J. Manuf. Mater. Process. **294**, 1–12 (2024).

[7]S. Shin, I. Jeon, and H. Sohn, "Enhanced geometric accuracy in directed energy deposition via closed-loop melt pool height control using real-time thermal imaging," Addit. Manuf. **109**, 104846 (2025).

[8]S. Webster, J. Jeong, J.-E. Mogonye, J. Zuback, S. Liao, J. Rocher, K. Ehmann, and J. Cao, "Effect of closed-loop coaxial melt pool temperature control on thermal history and microstructure of nickel alloy 718 in directed energy deposition," J. Mater. Process. Technol. **337**, 118725 (2025).

[9]Q. Wang, J. Li, A. R. Nassar, E. W. Reutzel, and F. Mitchell, "Model-based feedforward control of part height in directed energy deposition," Materials **14**, 337 (2021).

[10]J. Stoppok, D. Dillkötter, M. Thiele, C. Esen, S. Leonow, and M. Mönnigmann, "Working distance-based feedforward control of the weld bead height in directed energy deposition," IFAC-PapersOnLine **53**, 11806–11811 (2020).

[11]T. Ünal-Saewe, "Ortsaufgelöste Prozessüberwachung für die additive Fertigung mittels laserbasierter Directed Energy Deposition," Dr.-Ing. dissertation, 1. Auflage, Aachen, 2022.

[12]P. Rey, C. Prieto, C. González, K. Tzimanis, T. Souflas, P. Stavropoulos, J. S. Rathore, V. Bergeaud, C. Vienne, and P. Bredif, "Data analysis to assess part quality in DED-LB/M based on in-situ process monitoring," Procedia CIRP **111**, 345–350 (2022).

[13]M. Khanzadeh, S. Chowdhury, M. A. Tschopp, H. R. Doude, M. Marufuzzaman, and L. Bian, "In-situ monitoring of melt pool images for porosity prediction in directed energy deposition processes," IISE Trans. **51**, 437–455 (2019).

[14]T. Herzog, M. Brandt, A. Trinchi, A. Sola, C. Hagenlocher, and A. Molotnikov, "Defect detection by multi-axis infrared process monitoring of laser beam directed energy deposition," Sci. Rep. **14**, 3861 (2024).

[15]C. Hauschopp, S. Dicks, R. Kraft, J. Bremer, D. Wall, N. Brierley, and C. Häfner, "Multimodale Datenanalyse im Laserauftragschweißen - Analyse multimodaler und defektkorrelierter Daten als Grundlage für KI-gestützte Modelle," Werkstattstechnik Online **115**, 352–360 (2025).

[16]M. Mazzarisi, V. Errico, A. Angelastro, and S. L. Campanelli, "Influence of standoff distance and laser defocusing distance on direct laser metal deposition of a nickel-based superalloy," Int. J. Adv. Manuf. Technol. **120**, 2407–2428 (2022).